

PHASE-DEPENDENT PROPERTIES OF EXTRASOLAR PLANET ATMOSPHERES

TRAVIS S. BARMAN

Department of Physics and Astronomy, University of California at Los Angeles, Los Angeles, CA 90095
 Email: barman@astro.ucla.edu

PETER H. HAUSCHILDT

Hamburger Sternwarte, Gojenbergsweg 112, 21029 Hamburg, Germany
 Email: yeti@hs.uni-hamburg.de

FRANCE ALLARD

C.R.A.L (UML 5574) Ecole Normale Supérieure, 69364 Lyon Cedex 7, France
 Email: fallard@ens-lyon.fr

Received 2005 May 22; accepted 2005 June 27

ABSTRACT

Recently the Spitzer Space Telescope observed the transiting extrasolar planets, TrES-1 and HD209458b. These observations have provided the first estimates of the day side thermal flux from two extrasolar planets orbiting Sun-like stars. In this paper, synthetic spectra from atmospheric models are compared to these observations. The day-night temperature difference is explored and phase-dependent flux densities are predicted for both planets. For HD209458b and TrES-1, models with significant day-to-night energy redistribution are required to reproduce the observations. However, the observational error bars are large and a range of models remains viable.

Subject headings: Planets: exoplanets, radiative transfer

1. INTRODUCTION

Of the more than 100 extrasolar planetary systems discovered so far, only 7 have near edge-on orbits. These transiting planets are crucial for understanding giant planets in general since their masses and radii can easily be determined, and careful multi-wavelength observations can reveal some information about the planet's atmosphere (Brown et al. 2001; Charbonneau et al. 2002; Vidal-Madjar et al. 2003). Recently, two transiting planets, HD209458b and TrES-1, were observed with the Spitzer Space Telescope, providing the first direct measurements of their thermal flux. By comparing IR fluxes in and out of secondary eclipse (when the planet is behind the star), Charbonneau et al. (2005) measured the planet-star flux density ratio at 4.5 and 8 μm for TrES-1. Independently, Deming et al. (2005) measured the flux density ratio at 24 μm for HD209458b. These measurements provide the best constraints, so far, on the thermal structure and chemical composition of highly irradiated EGPs.

HD209458b and TrES-1 both have very short periods (just a few days) and orbital separations less than 0.05AU (Henry et al. 2000; Alonso et al. 2004). At such small orbital separations, they are substantially heated by radiation from their parent stars. Following the discovery of the planet around 51 Pegasi (Mayor & Queloz 1995), a variety of atmosphere models suitable for estimating the properties of these so-called “hot Jupiters” were published (Seager & Sasselov 1998; Barman et al. 2001; Sudarsky et al. 2003). However, since these planets probably have strong day-to-night photospheric differences, their potential lack of symmetry adds complications to an already difficult model atmosphere problem. Several of the most challenging issues are the cov-

erage and types of clouds (if present), redistribution of the absorbed stellar flux by atmospheric currents, depth dependent non-solar abundances, and photospheric temperature and pressure gradients from the day to night sides. These problems have been dealt with (or avoided) in a variety of ways and, therefore, a variety of model predictions exist.

New models, that estimate the horizontal atmospheric gradients under the assumption of radiative-convective equilibrium, are presented below. Several of the standard assumptions for global energy redistribution are explored. Model results are also compared to the most recent Spitzer measurements and estimates are given for the planet-star flux density ratios in the Spitzer 24 μm MIPS band and the four IRAC bands as a function of orbital phase.

2. MODEL CONSTRUCTION

The irradiated models presented below were calculated using the PHOENIX atmosphere code (Hauschildt & Baron 1999; Allard et al. 2001) adapted to include extrinsic radiation as described in Barman et al. (2001; here after BHA01, 2002). The spherically symmetric radiative transfer and chemical equilibrium equations were solved self-consistently, while explicitly accounting for the wavelength-dependent extrinsic radiation. The extrinsic radiation was also modeled with PHOENIX and, in each case, closely matches the observed parent star spectrum.

The major differences between the computation of the BHA01 models and those presented here lie with the treatment of dust in the atmosphere and the assumptions concerning the redistribution of absorbed stellar flux over the planet's day and night hemispheres.

TABLE 1. MODEL PARAMETERS

		HD209458b [†]	TrES-1 [‡]
T_* (K)	...	6088 ± 56	5250 ± 75
R_* (R_\odot)	...	1.145 ± 0.049	0.83 ± 0.05
M_* (M_\odot)	...	1.06	0.89
R_p (R_{Jup})	...	$1.42^{+0.10}_{-0.13}$	$1.04^{+0.08}_{-0.05}$
M_p (M_{Jup})	...	0.69	0.76
a (AU)	...	0.0468	0.0393

REFERENCES. — (†) Ribas et al. (2003), Cody & Sasselov (2002); (‡) Sozzetti et al. (2004)

2.1. Cloud-free Assumption

Unlike many brown dwarfs, EGP’s do not necessarily have convective photospheres. For EGP’s with small orbital separations, irradiation can suppress convection to depths well below the photosphere, leading to a fully radiative atmosphere across most of the day side (Guillot et al. 1996). Since radiative photospheres have short sedimentation time-scales, cloud growth should be difficult to sustain making the cloud-free assumption reasonable. However, this assumption may break down if strong zonal winds are present and advective time-scales are comparable to sedimentation time-scales. The efficiency of gravitational settling will also depend on the poorly constrained eddy diffusion coefficient (Rossow 1978).

In BHA01, cloud-free atmospheres were modeled using the “Cond” opacity setup (Allard et al. 2001). The Cond setup accounts for dust formation in the atmosphere, as determined by chemical equilibrium equations, but excludes the dust opacity when computing the thermal and spectroscopic properties of the atmosphere. Excluding the dust opacity was intended to approximate the effects of cloud formation followed by efficient gravitational settling (often referred to as “Rainout”) which acts to deplete an atmosphere of many important refractory elements. Rainout and the depletion of refractory elements have been recognized for some time as important processes in the atmospheres of Jovian planets and brown dwarfs (Fegley & Lodders 1996; Lodders 1999; Burrows et al. 2000; Marley et al. 2002). The success of these models is strong motivation for exploring the rainout assumption in extrasolar planet atmospheres.

While the Cond approximation does effectively remove refractory elements, it does not alter the overall abundance of an element sequestered by grain formation at a given temperature and pressure. Grain formation and efficient gravitational settling alter the abundance of an element by continually removing the refractory elements that make up a grain until the grain is no longer able to form due to a lack of one or more constituents. In the absence of replenishment (e.g., by convective updrafts), certain layers of an atmosphere where only gravitational settling has occurred will not only be free of dust species but also free of a significant number of metals and related molecules. For a description of this effect in Jupiter’s atmosphere, see Lodders (1999).

The Cond case, therefore, does not go far enough in removing refractory elements from the upper atmosphere

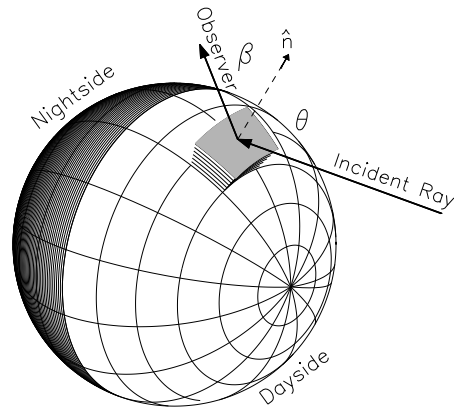


FIG. 1.— Illustration of the planet’s hemisphere divided into small regions, each to be modeled independently. Each concentric band around the sub-stellar point (depicted here as the convergence point of longitudinal lines) receives the same amount of incident stellar flux at the same incident angle. Therefore, each band is assumed to have the same atmospheric structure and emergent intensities. The angle between the incident ray and the outward pointing surface normal is θ . When computing the emergent flux, only those intensities aligned with the observer line-of-sight are integrated over the visible hemisphere. The angle between the surface normal and an observer’s line-of-sight is β .

and can lead to a small concentration of key absorbers like TiO and VO that are important in irradiated atmospheres. These two molecules have strong absorption bands near the peak flux densities of solar type stars. Consequently, their presence or absence can greatly affect the depth at which the stellar flux is absorbed in the planet’s atmosphere and, thus, alter the predicted atmospheric structure (Hubeny et al. 2003).

In this work, an improved cloud-free model was used that iteratively reduces (at a given layer) the elemental abundances involved in grain formation and recomputes the chemical equilibrium with each new set of stratified elemental abundances. This model is similar to the Rainout model of Burrows & Sharp (1999), except that the depletion of elements is continued until grains (and thus grain opacities) are no longer present (see also Allard et al. (2003) for more details). The resulting equilibrium chemistry and opacity sampling of this cloud-free model are fully self-consistent, unlike the earlier Cond models which simply excluded the grain opacity. Also, for the models described below, Ti and V were significantly depleted from the photosphere by the rainout process leading to negligible concentrations of TiO and VO. For a detailed discussion of the differences between Rainout and Cond irradiated models, see Barman et al. (2005, in preparation).

2.2. Modeling the Day-Night Gradients

The majority of static atmosphere models arrive at a single temperature-pressure (T-P) profile intended to represent an average of either the day side or over the entire planet (Seager & Sasselov 1998; Goukenleuque et al. 2000; Barman et al. 2001; Sudarsky et al. 2003). However, if most short period planets are well represented by a static atmosphere in radiative-convective equilibrium, then one should expect them to have a horizontal (day-to-night) temperature gradient – simply due to the

center-to-limb variation in the amount of incident stellar flux received by the planet. In the absence of a 3-D model atmosphere code, one approach that comes closer to the real solution is to divide a planet's day side into a series of concentric regions around the sub-stellar point. In the static case, suitably large regions should interact very little via radiative transfer processes, except perhaps near the terminator.

The planetary atmospheres described below were modeled by dividing the day side into 10 concentric regions defined by $\mu = \cos(\theta)$, where θ is the angle between the surface normal and the direction to the star (see Fig. 1). For these regions, μ ranged from 1.0 (at the sub-stellar point) to 0.1 (the model region closest to the terminator), in steps of $\Delta\mu = 0.1$. The corresponding T-P profiles and emergent intensities were modeled using 1-D, spherically symmetric, atmospheres each receiving incident stellar flux along the appropriate angle for a given region. For these day side models, the radiative transfer equation was modified so that the incident specific intensities along any μ and azimuthal angle ϕ were given by,

$$I_{inc,\lambda}(\mu, \phi) = I_{o,\lambda} \delta(\mu - \mu') \delta(\phi - \phi'), \quad (1)$$

with δ being the Dirac delta function. In which case, it follows that the incident fluxes are simply,

$$F_{inc,\lambda}(\mu) = \mu I_{o,\lambda} = \mu \left(\frac{R_\star}{d} \right)^2 F_{\star,\lambda}, \quad (2)$$

where $F_{\star,\lambda}$ are the monochromatic fluxes from the star's surface, R_\star is the stellar radius, and d is the distance from the stellar surface to the planet's atmosphere. For the night side, a single, non-irradiated, model was used.

All models were solved self-consistently so that each μ -region had a chemistry characterized by its T-P profile. By having chemical equilibria consistent with the T-P profiles across the planet's atmosphere, this approach naturally leads to variations in the important photospheric opacity sources from the day to night side – an important aspect when computing the synthetic spectra.

Since EGPs are believed to have fully convective interiors, the *intrinsic* effective temperature (T_{int})¹ for each modeled region was adjusted so that, after convergence, all T-P profiles reached the same adiabat below the photosphere². The adiabat was selected based on planetary interior and evolution calculations for a given mass, age, metallicity, and irradiation (Baraffe et al. 2003, 2004; Chabrier et al. 2004). This entropy matching technique has also been used for irradiated binary stars and allows one to assign models with different intrinsic luminosities to different regions of the same star or planet (Vaz & Nordlund 1985; Nordlund & Vaz 1990; Barman et al. 2004).

The monochromatic fluxes from the model planet were obtained by integrating the emergent intensities along an observer's line-of-sight (*los*) for a given observer-planet-

star orientation.

$$F_{los,\lambda} = \int_{los} I_\lambda(\theta, \phi) d\Omega. \quad (3)$$

The integration was performed by distributing ~ 2000 points over the entire surface with corresponding cubature integration weights (w_i). The distribution of points was determined by the minimization of potential energy on the unit sphere. This distribution is nearly orientation independent, unlike the standard latitude-longitude grid, and results in very small integration errors (Steinacker et al. 1996; Sloan & Womersley 2001). Each point on the observer-facing hemisphere was assigned an emergent intensity spectrum corresponding to the angle, β , between the observer's *los* and the surface normal (see Fig. 1), and depending on the day or night region in which the point belonged. Numerical integration of Eq. 3 becomes a sum over the visible points,

$$F_{los,\lambda} = \sum_{i(\text{visible})} w_i \mu_i I_\lambda(\mu_i). \quad (4)$$

In Eq. 4, $\mu = \cos(\beta)$ and is not to be confused with the 10 μ values used to divide the day hemisphere. With this technique, the phase-dependent spectra can be estimated while taking into account the center-to-limb variation of the planet's emergent intensities – which might include a combination of limb brightening and darkening. The emergent intensities were sampled over 114 directions per μ -region and were assumed to be azimuthally symmetric about the surface normal. Assuming azimuthal symmetry is justified since the present work is concerned primarily with the thermal flux, not scattered light. Phase-dependent optical spectra will be explored in a later paper.

The simple approach outlined above has several limitations. Since radiation passing through one region into another is neglected, heating of the upper atmosphere near the terminator may be underestimated at low gas pressures. However, this is unlikely to affect the emergent thermal IR spectrum that forms deeper in the atmosphere. It has also been assumed that the planet is tidally locked and, hence, presents a constant face to the parent star. The models are also time-independent and static and, consequently, neglect the effects of zonal winds that could change the thermal profiles by coupling the hot day side to the cooler night side.

2.3. Energy Redistribution

The approach outlined in the previous section is designed to model the planet's atmosphere under the assumption that the gas is truly static and in radiative-convective equilibrium. As such, this approach will predict the maximum heating at the sub-stellar point and very little heating at the terminator. However, as mentioned above, an important consequence of stellar heating is horizontal atmospheric flows capable of transporting appreciable amounts of energy to the night side. The impacts of horizontal motion on EGP atmospheres have been modeled by a variety of groups, each predicting some level of atmospheric circulation that depends strongly on adopted opacities and general approaches to the problem (Showman & Guillot 2002; Cho et al. 2003; Burkert et al. 2005; Cooper & Showman 2005). Despite

¹ In the present work, T_{int} characterizes the intrinsic luminosity of an irradiated model atmosphere, defined by $4\pi R_p^2 \sigma T_{\text{int}}^4$. For non-irradiated models, the normal T_{eff} is used to describe the flux and luminosity.

² The region referred to as the photosphere lies roughly between $P = 0.01$ and 1 bar, corresponding to where the optical depth at IR wavelengths is near unity.

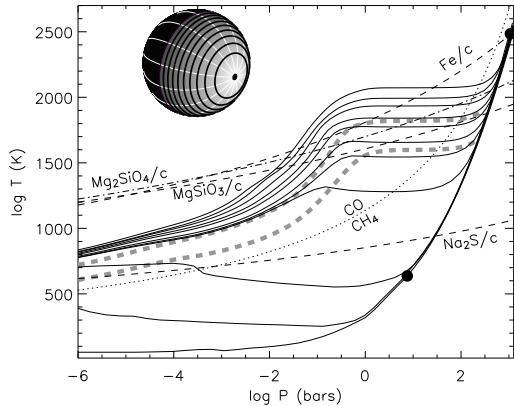


FIG. 2.— Temperature versus pressure for a sequence of irradiated atmospheres. For each model, the parameters for TrES-1 from Table 1 were chosen and only the direction of the incident flux relative to the surface normal was varied. From top to bottom, the models have $\mu = 1.0$ to $\mu = 0.1$ in steps of 0.1. The dashed lines indicate the approximate condensation curves for three common grain species. The dotted line indicates where gaseous CO and CH₄ concentrations are equal (CO is dominant to the left of this line). The approximate regions represented by the collection of T-P profiles are shown as solid black lines on the illustrative sphere. The top-most T-P profile corresponds to the sub-stellar point (black dot on the sphere). The terminator and night side (black hemisphere) are modeled with the non-irradiated profile (lowest T-P curve). The radiative-convective boundary at the sub-stellar point and on the night side are labeled with filled circles. The thick, grey, dashed lines are T-P profiles for $\alpha = 0.5$ (top) and $\alpha = 0.25$ (bottom) models.

the differences in methods and results, the general consensus from these hydrodynamic simulations is that circulations can redistribute a fraction of the incident energy over large portions of a strongly irradiated planetary atmosphere.

For single, 1-D, model atmospheres designed to reproduce the detailed chemistry, opacities, and emergent spectrum (but not the atmospheric motions), the effects of energy redistribution have been folded into a single parameter, referred to as α in this work. The α parameter is simply the ratio of the planet’s cross-sectional area (πR_p^2) and the surface area of the planet from which the absorbed stellar luminosity is to be re-emitted. In this case, the stellar flux incident at the top of the model atmosphere becomes,

$$F_{\text{inc},\lambda} = \alpha \left(\frac{R_\star}{d} \right)^2 F_{\star,\lambda}. \quad (5)$$

For a more detailed description of the energy balance in an irradiated binary companion and the development of a similar α parameter, see Paczyński (1980).

When the incident flux is scaled by α , the underlying assumption is that dynamical processes in the atmosphere are efficient enough to uniformly distribute the incident luminosity over either the day hemisphere ($\alpha = 0.5$) or the entire sphere ($\alpha = 0.25$). In addition, every point on the day side (or entire surface) is assumed to be identical and, thus, can be described by a single 1-D model with the same emergent and incident flux. Note that the $\alpha = 0.5$ case corresponds to the average (over μ) of the incident flux defined in Eq. 2. Also, the no-redistribution and $\alpha = 0.5$ cases receive and re-

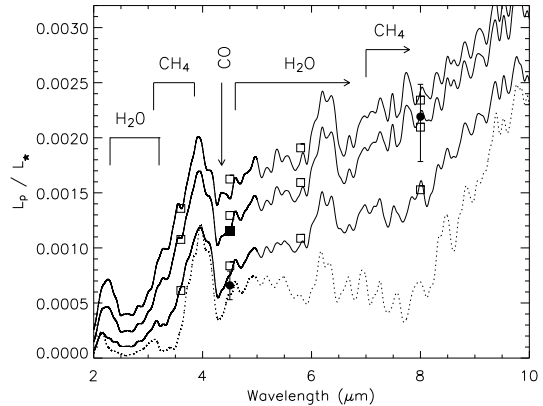


FIG. 3.— Planet-star flux density ratios for day side models assuming no redistribution (top curve) and redistribution models with $\alpha = 0.5$ (middle solid curve) and $\alpha = 0.25$ (bottom solid curve). The model T-P profiles are shown in Fig. 2. IRAC band fluxes for each model (found by convolving with the IRAC response curves) are indicated with open squares and filled circles show the Spitzer data with 1σ error bars. The $4.5 \mu\text{m}$ IRAC value for a $10\times$ solar, $\alpha = 0.5$, model is also shown (solid square). The lower dotted line corresponds to an isolated brown dwarf model with $T_{\text{eff}} = 1150 \text{ K}$.

radiate the same amount of incident luminosity from the day side, but will predict very different T-P profiles and phase-dependent spectra (see below).

3. RESULTS

The greatest number of observational constraints exists for the planets TrES-1 and HD209458b. Models specifically tailored for these two objects are presented below, adopting the parameters listed in Table 1, and are compared to the recent Spitzer data.

3.1. TrES-1

Figure 2 shows the sequence of solar metallicity T-P profiles across the day and night sides of TrES-1. On the day side, $T_{\text{int}} \sim 100\text{K}$ which is motivated by evolution calculations that reproduce the observed radius of TrES-1 (Baraffe et al. 2005). The night side atmosphere model with the same adiabat as the day side, has $T_{\text{eff}} = 225\text{K}$ based on the entropy matching criteria mentioned above. The sphere in Fig. 2 shows the concentric regions around the sub-stellar point represented by each atmosphere model.

As expected, a steep temperature gradient along an isobar, $\nabla T_P = (\partial T / \partial \mu)_P$, is present from the sub-stellar point to the terminator. At $P > 0.01 \text{ bar}$, ∇T_P is very large across most of the day side and increases dramatically as the temperatures drop off near the terminator (designated by the night side T-P profile). Unlike the deeper layers, the top most layers of the atmosphere receive a steady supply of incident stellar flux, even when $\alpha > 60^\circ$ – however at shallow angles with respect to the surface normal. Consequently, ∇T_P is smaller for $P < 0.01 \text{ bar}$ compared to higher pressure depths for most of the day side except near the terminator. Note also that the T-P profiles (for large α) become flatter at low P and steeper at high P and, eventually, become inverted very near the terminator.

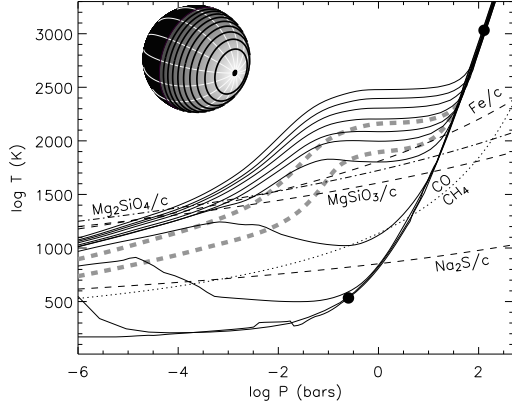


FIG. 4.— Same as Fig. 2 but adopting the parameters for HD209458b in Table 1.

The stellar heating also causes the atmospheric extension³ to increase from the terminator to the sub-stellar point by a factor of ~ 5 . The change in extension coincides with a significant pressure gradient below the photosphere along constant-height surfaces where the change in pressure from the day to night side can be factors as large as 50 to 100. Above the photosphere, the day-to-night pressure gradient is present, but fairly small. Despite the large increase in extension, the change in radius is modest leading to no more than a 5% increase in the area of an isobaric surface on the day side compared to the night. Also of interest is the radiative-convective boundary which is not on an isobar and is significantly deeper at the sub-stellar point ($P \sim 10^3$ bar) compared to the terminator and night side ($P \sim 10$ bar).

The condensation curves for Fe, Mg_2SiO_4 , MgSiO_3 and Na_2S are also shown in Fig. 2. Cloud formation is typically believed to occur near the intersection of the T-P profile and the condensation curve for a given species. While the models presented here are cloud-free, the condensation curves suggest that photospheric clouds might be possible at a variety of atmospheric depths and compositions but, in the no-redistribution case, would be confined to $\sim 50\%$ of the day side around the sub-stellar point. The no-redistribution model also suggests that clouds might form at much greater heights (i.e. lower P) around the sub-stellar point compared to the $\alpha = 0.5$ redistribution model. The presence of clouds would have an impact on the predicted T-P profile and, therefore, needs to be treated self-consistently. Cloud formation across the day and night sides will be explored in a future paper.

The high day side temperatures lead to an atmospheric chemistry dominated by H_2 , He, H_2O and CO. However, near the terminator and on the night side, most of the carbon is bound in CH_4 . In Fig. 3, the planet-star flux

³ The atmospheric extension is defined here as the difference between the radius at $P = 10^{-6}$ bar and at $P = 100$ bar.

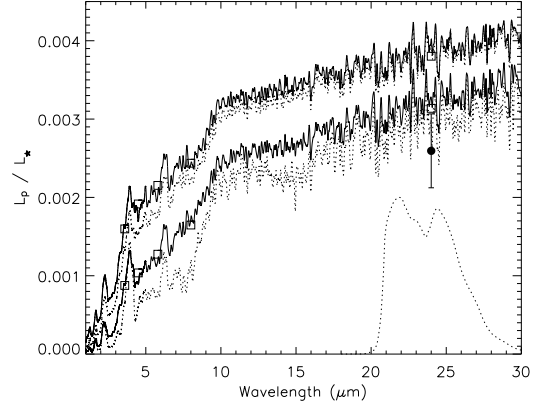


FIG. 5.— Planet-star flux density ratio for HD209458b assuming no redistribution (top solid curve) and redistribution models with $\alpha = 0.5$ (top dotted curve) and $\alpha = 0.25$ (bottom solid curve). The T-P profiles are shown in Fig. 4. Open squares indicate the predicted IRAC and MIPS flux densities. The observed $24 \mu\text{m}$ MIPS value is shown with 1σ error bars (filled circle) along with the $24 \mu\text{m}$ MIPS response curve. The lower dotted line is the flux density ratio for a Brown Dwarf with $T_{\text{eff}} = 1450\text{K}$.

density ratios⁴,

$$\frac{L_p}{L_*} = \left(\frac{R_p}{R_*} \right)^2 \frac{F_p}{F_*}, \quad (6)$$

for the no-redistribution model are compared to the Spitzer observations along with standard 1-D models with $\alpha = 0.5$ and $\alpha = 0.25$. Since the stellar spectrum at IR wavelengths is fairly smooth, all of the features seen are due to absorption in the planet's day side photosphere. Strong absorption by H_2O and CO are easily identified in the model. The two hottest models (no redistribution and $\alpha = 0.5$) are in good agreement with the observations at $8 \mu\text{m}$ but significantly overestimate the flux density at $4.5 \mu\text{m}$. The models with complete redistribution ($\alpha = 0.25$) agrees reasonably well at $4.5 \mu\text{m}$ and, at the 2σ level, agrees with the $8 \mu\text{m}$ observations. Despite the broad wavelength span of the IRAC instrument, all of the IRAC bands probe a fairly narrow region of the planetary atmosphere between $P = 10^{-1}$ and 10^{-2} bar.

Also shown in Fig. 3 are the flux density ratios using a spectrum from a non-irradiated brown dwarf model atmosphere with $T_{\text{eff}} = 1150\text{K}$ which roughly corresponds to the equilibrium T_{eff} of the $\alpha = 0.25$ model. While models of brown dwarfs appear to agree very well with recent Spitzer IRS spectra of L and T dwarfs (Roellig et al. 2004), the observations of TrES-1 are clearly inconsistent with a standard brown dwarf spectrum, especially around $8 \mu\text{m}$. This disagreement confirms that irradiated EGPs have atmospheric structures very different from isolated brown dwarfs⁵; a property that was not immediately obvious in the past.

⁴ The ratio $(R_p/R_*)^2$, determined from the transit light curves, has error bars much smaller than the individual planet or stellar radii. Therefore, the flux density ratio comparison is not limited by the typical uncertainties of an absolute flux determination.

⁵ Fortney et al. (2005) have also commented on the less than satisfactory agreement between models and the EGP Spitzer data in light of the very good agreement between models and Spitzer IRS brown dwarf spectra.

As demonstrated by our own solar system planets, it is possible that EGPs do not have the same metal abundances (or relative proportions) as their parent star. The main discrepancy between the no-redistribution and $\alpha = 0.5$, solar abundance, models is the $4.5 \mu\text{m}$ flux which coincides with the strong fundamental CO absorption band. The flux density ratio could be low at these wavelengths due to enhanced metal abundances. In order to achieve a CO absorption feature with flux density ratios as low as in the $\alpha = 0.25$ solar abundance model (which reproduces the $4.5 \mu\text{m}$ IRAC observations), the metal abundance would have to be 10 times that of the parent star (see Fig. 3). However, given the width of the IRAC band passes, the fluxes outside the CO absorption band remain high enough to keep the model's integrated flux density ratio above the 2σ error bar. Note that increasing the C to O ratio does not improve the comparison to observations. A larger C to O ratio increases CO absorption, but simultaneously lowers the water concentration thereby increasing the planet's fluxes at wavelengths red-ward of the $4.5 \mu\text{m}$ that are also included in the IRAC band.

3.2. HD209458b

Figure 4 shows the T-P profiles for HD209458b assuming solar abundances, and the parameters listed in Table 1. The adopted inner adiabat was based on evolution calculations which suggest a substantial intrinsic luminosity for HD209458b's mass and abnormally large radius (Baraffe et al. 2003). The sub-stellar point $T_{\text{int}} = 230\text{K}$ and the entropy-matching non-irradiated model for the terminator and night side has $T_{\text{eff}} = 500\text{K}$.

The predicted T-P trend across the day side is similar to that for TrES-1. The major differences are due to the greater parent star luminosity for HD209458b, which leads to a significantly hotter sub-stellar point. The intrinsic luminosity is also higher for HD209458b, which leads to warmer regions near the terminator. The decline in temperature above the nearly isothermal photosphere ($P < 0.01$ bar) for the hottest portions of the dayside is consistent with recent works by other groups (Sudarsky et al. 2003; Fortney et al. 2005; Iro et al. 2005). This temperature decline points to some of the differences mentioned above between the present Rainout models and those based on the earlier Cond approximation. For HD209458b, with $\alpha = 0.5$, the Cond assumption leads to a nearly isothermal profile ($T \sim 1700\text{K}$) for most of the atmosphere (see Fig. 2 of Chabrier et al. (2004)). While the complete removal of TiO and VO via the adopted Rainout process contributes to the cooler outer atmosphere and hotter photosphere shown in Fig. 4. A more detailed comparison between Rainout and Cond models is given in Barman et al. (2005, in preparation).

If clouds are sustainable on the planet's day side, then Fe, MgSiO_3 and Mg_2SiO_4 clouds might form at very low pressures across most of the day side surrounding the sub-stellar point. Near the terminator, the temperatures are much cooler than the average temperature across the day side. Consequently, most of the limb is well below the condensation temperature of Na, consistent with the findings by Iro et al. (2005). Condensation of Na near the limb may contribute to the lower than expected Na absorption detected with HST (Charbonneau et al.

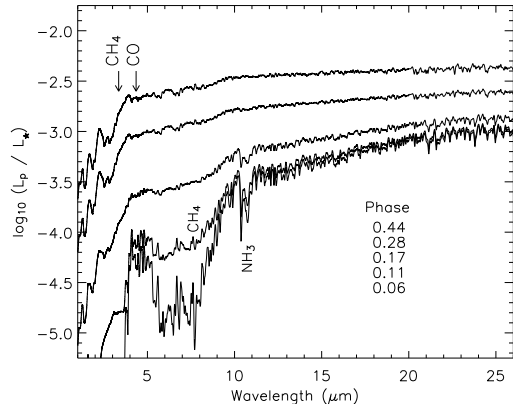


FIG. 6.— Planet-star flux density ratios for HD209458b assuming no redistribution at five different orbital phases from 0.44 (top curve) to 0.06 (bottom curve) and orbital inclination of 90° . Phase = 0 coincides with the time of transit and only the night side is visible. At phase = 0.5 the planet is behind the star.

2002).

The $24 \mu\text{m}$ MIPS observations probe the Rayleigh-Jeans tail of the planet's spectrum, in a region dominated by H_2O line opacity. Figure 5 shows the day side planet-star flux density ratios for the no-redistribution model and 1-D models with $\alpha = 0.25$ and $\alpha = 0.50$. At the 1σ level, the MIPS observations favor a strong redistribution of the absorbed stellar flux ($\alpha = 0.25$). The two hottest cases, no redistribution and $\alpha = 0.5$, are only marginally in agreement with the 2σ observational error bars. The MIPS observation probes the atmosphere at a pressure ($P \sim 10^{-2}$) similar to those probed by the IRAC observations. Note also that for $\lambda > 10 \mu\text{m}$, the planet's day side spectrum is nearly identical to that of a non-irradiated brown dwarf with $T_{\text{eff}} = 1450\text{K}$ (which matches the emergent flux for the $\alpha = 0.25$ case). The brown dwarf-like appearance of the spectrum at far-IR wavelengths is to be expected since, at these temperatures, $24 \mu\text{m}$ is well within the Rayleigh-Jeans tail.

Another potentially useful limit for HD209458b has been set at shorter wavelengths by ground based observations (Richardson et al. 2003; Seager et al. 2005). These observations indicate the planet's spectrum may have a less prominent $2.2 \mu\text{m}$ peak (or an overall lower luminosity) than predicted by many models. This limit also favors $\alpha < 0.50$.

3.3. Phase-dependent Flux densities

Since the entire day hemisphere has been modeled by a collection of T-P profiles and intensity spectra, estimates for the phase-dependent fluxes can be constructed simply by changing the star-planet-observer orientation and re-integrating the surface intensities (see Eqs. 3 and 4). Figure 6 shows the predicted phase-dependent flux density ratios for HD209458b with no energy redistribution. Note the significant drop in flux between 5 and $10 \mu\text{m}$ and the shift in the peak flux between 1 and $8 \mu\text{m}$ toward redder wavelengths. As the phase approaches zero, the coolest parts of the planet, which are dominated by CH_4 absorption, come into view.

Flux densities for IRAC and $24 \mu\text{m}$ MIPS bands are shown in Fig. 7 for all phases with ($\alpha = 0.5$ and 0.25) and

without energy redistribution. As the level of redistribution increases, the thermal surface brightness becomes more uniform and the IR light-curves flatten out. For $\alpha = 0.25$, the IR light-curves are constant with values equal to those shown in Fig. 3. Note that optical and near-IR light-curves will not be flat when $\alpha = 0.25$ due to reflected star light.

A phase shift of TrES-1's hot side would not improve the simultaneous fitting of no-redistribution and $\alpha = 0.5$ models to the 1σ observed 8 and $4.5 \mu\text{m}$ fluxes for TrES-1. For HD209458b, both $\alpha = 0.25$ and 0.5 models agree with the 2σ error bars but favor $\alpha = 0.25$ at the 1σ level. However, the large 2σ error bars do leave room for a shift of up to 0.25 in phase – similar to recent results from atmospheric circulation models (Cooper & Showman 2005). For both planets, the best fitting model appears to be one with $\alpha = 0.25$. This may indicate that fast photospheric winds are present with speeds in excess of 1 km s^{-1} as predicted for atmospheres with similar day-night temperature differences (Cooper & Showman 2005). However, using approximations for the radiative and advective time-scales (Showman & Guillot 2002; Seager et al. 2005) and assuming 1 km s^{-1} wind speeds, $\tau_{\text{rad}}/\tau_{\text{adv}} < 1$ for $P < 1 \text{ bar}$ at the sub-stellar point for both TrES-1 and HD209458b. Small values for τ_{rad} suggest that winds will not be capable of entirely removing the large day-night temperature differences even at photospheric depths.

4. DISCUSSION AND CONCLUSIONS

Detailed radiative-convective equilibrium models have been presented above for the atmospheres of HD209458b and TrES-1. In the absence of energy redistribution, the models predict steep horizontal temperature gradients from the sub-stellar point to the night side that vary substantially with depth. Compared to earlier works, which assumed very efficient energy redistribution, the no-redistribution models predict much hotter temperatures across most of the day hemisphere and significantly cooler temperatures near the terminator.

The existence of steep horizontal temperature gradients in equilibrium models strengthens the case for strong zonal winds. However, fast winds ($\sim 2 \text{ km sec}^{-1}$) capable of altering the global atmospheric temperature profile are unlikely to entirely remove these temperature gradients, especially at pressures lower than a bar (Cooper & Showman 2005; Iro et al. 2005). Since τ_{rad} decreases rapidly with decreasing pressure (i.e. towards the top of the atmosphere), the horizontal and vertical temperature gradients may well have a mixture of the T-P characteristics shown above for the various redistribution scenarios. For example, the temperature structures could be close to the static, no-redistribution, scenario at $P < 0.01 \text{ bar}$ where $\tau_{\text{rad}} < 10^4 \text{ sec}$. Deeper into the atmosphere (where $\tau_{\text{rad}} \gg \tau_{\text{adv}}$) advection is probably an important mechanism for energy transport which could lead to a T-P structure similar to that of an $\alpha = 0.5$ or $\alpha = 0.25$ redistribution model for $P > 1 \text{ bar}$. Consequently, the T-P profile could, in some cases, be fairly flat across much of the day side photosphere. Note that a flat

photospheric T-P profile would produce a spectrum close to that of a blackbody – a possibility which, so far, is not excluded by Spitzer observations (see Charbonneau et al. (2005) for a blackbody comparison to the TrES-1 Spitzer data).

The $24 \mu\text{m}$ Spitzer observations of HD209458b have been shown to favor an atmosphere undergoing efficient day-to-night energy redistribution. The 4.5 and $8.0 \mu\text{m}$ observations of TrES-1 also favor an atmosphere which is experiencing significant redistribution. However, an $\alpha = 0.25$ redistribution model only agrees with both data points, simultaneously, at the 2σ level. For both planets, it appears that the fully static, no-redistribution, case is ruled out by the Spitzer data. However, the data points are too few and have error bars that are too large to significantly constrain the model parameters.

In anticipation of additional Spitzer observations, phase-dependent spectra have been calculated, along with phase-dependent planet-star flux density ratios. For HD209458b, placing limits on the fluxes at the quadrature and near night side phases (esp. at $24 \mu\text{m}$) would test the large night side luminosity (with $T_{\text{eff}} \sim 400 - 500 \text{ K}$) predicted by evolution calculations. The ratios of the planet's flux densities at phases 0.5 and 0.25 could also further constrain the degree to which energy is redistributed to the night side.

The current work is also applicable to planets in non-transiting orbits. There is a direct correspondence between the phase-dependent fluxes shown above (for an edge-on orbit) and the *inclination*-dependent fluxes for a planet at superior conjunction in an arbitrarily inclined orbit. Therefore, the predictions made above suggest that Spitzer could detect flux variations due to a close-in planet with orbital inclination as small as 45° (i.e., phase 0.375 or 0.625 in Fig. 7). Since only two of the known transiting planets orbit stars bright enough to measure the planet-star flux density ratios, performing similar observations as Deming et al. (2005) and Charbonneau et al. (2005) for non-transiting planets orbiting nearby stars would be very helpful.

We thank Isabelle Baraffe, Gilles Chabrier and Brad Hansen for their useful comments and suggestions. We also thank Dave Charbonneau and Sara Seager for providing pre-prints of their recent papers and the anonymous referee for his/her efforts. This research was supported by NASA through LTSA grant NAG5-3435 to Wichita State University and Origins of Solar Systems grant NNG04GL86G to University of California at Los Angeles. We also acknowledge support by the CNRS. TSB acknowledges additional support by NASA through the AAS small research grant program and PHH was supported in part by the Pôle Scientifique de Modélisation Numérique at ENS-Lyon. Some of the calculations were performed on the IBM pSeries of the HLRN and CINES, the IBM SP of the NERSC, the WSU HIPECC, and on NASA's Project Columbia computer system. We thank all these institutions for a generous allocation of computer time.

REFERENCES

- Allard, F., Guillot, T., Ludwig, H., Hauschildt, P. H., Schweitzer, A., Alexander, D. R., & Ferguson, J. W. 2003, in IAU Symposium, 325–
 Allard, F., Hauschildt, P. H., Alexander, D. R., Tamanai, A., & Schweitzer, A. 2001, ApJ, 556, 357

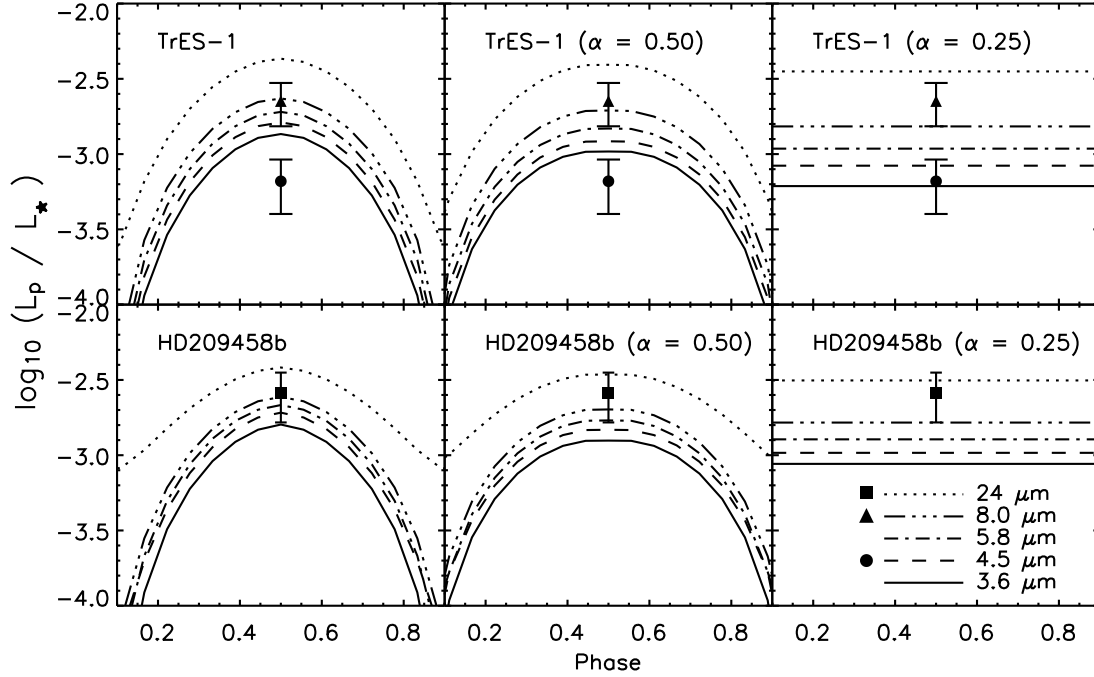


FIG. 7.— Phase-dependent flux density ratios for the 24 μm MIPS band and the four IRAC bands for TrES-1 and HD209458b. Model calculations with no redistribution are shown in the left column. Results for models with redistribution characterized by $\alpha = 0.5$ and 0.25 are shown in the middle and right columns. The Spitzer observations are shown as filled symbols with 2σ error bars. Each data point should be compared to only one of the theoretical light-curves (see legend for the symbol-linestyle relation). At phase = 0.5, only the day side is visible.

- Alonso, R., Brown, T. M., Torres, G., Latham, D. W., Sozzetti, A., Mandushev, G., Belmonte, J. A., Charbonneau, D., Deeg, H. J., Dunham, E. W., O'Donovan, F. T., & Stefanik, R. P. 2004, *ApJ*, 613, L153
- Baraffe, I., Chabrier, G., Barman, T. S., Allard, F., & Hauschildt, P. H. 2003, *A&A*, 402, 701
- Baraffe, I., Chabrier, G., Barman, T. S., Selsis, F., Allard, F., & Hauschildt, P. H. 2005, *A&A*, 436, L47
- Baraffe, I., Selsis, F., Chabrier, G., Barman, T. S., Allard, F., Hauschildt, P. H., & Lammer, H. 2004, *A&A*, 419, L13
- Barman, T. S., Hauschildt, P. H., & Allard, F. 2001, *ApJ*, 556, 885
- , 2004, *ApJ*, 614, 338
- Barman, T. S., Hauschildt, P. H., Schweitzer, A., Stancil, P. C., Baron, E., & Allard, F. 2002, *ApJ*, 569, L51
- Brown, T. M., Charbonneau, D., Gilliland, R. L., Noyes, R. W., & Burrows, A. 2001, *ApJ*, 552, 699
- Burkert, A., Lin, D. N. C., Bodenheimer, P. H., Jones, C. A., & Yorke, H. W. 2005, *ApJ*, 618, 512
- Burrows, A., Guillot, T., Hubbard, W. B., Marley, M. S., Saumon, D., Lunine, J. I., & Sudarsky, D. 2000, *ApJ*, 534, L97
- Burrows, A. & Sharp, C. M. 1999, *ApJ*, 512, 843
- Chabrier, G., Barman, T., Baraffe, I., Allard, F., & Hauschildt, P. H. 2004, *ApJ*, 603, L53
- Charbonneau, D., Allen, L. E., Megeath, S. T., Torres, G., Alonso, R., Brown, T. M., Gilliland, R. L., Latham, D. W., Mandushev, G., O'Donovan, F. T., & Sozzetti, A. 2005, *ApJ*, 626, 523
- Charbonneau, D., Brown, T. M., Noyes, R. W., & Gilliland, R. L. 2002, *ApJ*, 568, 377
- Cho, J. Y.-K., Menou, K., Hansen, B. M. S., & Seager, S. 2003, *ApJ*, 587, L117
- Cody, A. M. & Sasselov, D. D. 2002, *ApJ*, 569, 451
- Cooper, C. S. & Showman, A. P. 2005, *ApJ*, in press
- Deming, D., Seager, S., Richardson, L. J., & Harrington, J. 2005, *Nature*, 434, 740
- Fegley, B. J. & Lodders, K. 1996, *ApJ*, 472, L37
- Fortney, J. J., Marley, M. S., Lodders, K., Saumon, D., & Freedman, R. 2005, *ApJ*, in press
- Goukenleuque, C., Bézard, B., Jorget, B., Lellouch, E., & Freedman, R. 2000, *Icarus*, 143, 308
- Guillot, T., Burrows, A., Hubbard, W. B., Lunine, J. I., & Saumon, D. 1996, *ApJ*, 459, L35
- Hauschildt, P. H. & Baron, E. 1999, *JCAM*, 109, 41
- Henry, G. W., Marcy, G. W., Butler, R. P., & Vogt, S. S. 2000, *ApJ*, 529, L41
- Hubeny, I., Burrows, A., & Sudarsky, D. 2003, *ApJ*, 594, 1011
- Iro, N., Bézard, B., & Guillot, T. 2005, *A&A*, 436, 719
- Lodders, K. 1999, *ApJ*, 519, 793
- Marley, M. S., Seager, S., Saumon, D., Lodders, K., Ackerman, A. S., Freedman, R. S., & Fan, X. 2002, *ApJ*, 568, 335
- Mayor, M. & Queloz, D. 1995, *Nature*, 378, 355
- Nordlund, A. & Vaz, L. P. R. 1990, *A&A*, 228, 231
- Paczynski, B. 1980, *Acta Astronomica*, 30, 113
- Ribas, I., Solano, E., Masana, E., & Giménez, A. 2003, *A&A*, 411, L501
- Richardson, L. J., Deming, D., & Seager, S. 2003, *ApJ*, 597, 581
- Roellig, T. L., Van Cleve, J. E., Sloan, G. C., Wilson, J. C., Saumon, D., Leggett, S. K., Marley, M. S., Cushing, M. C., Kirkpatrick, J. D., Mainzer, A. K., & Houck, J. R. 2004, *ApJS*, 154, 418
- Rossow, W. B. 1978, *Icarus*, 36, 1
- Seager, S., Richardson, L. J., Hansen, B. M. S., Menou, K., Cho, J. Y.-K., & Deming, D. 2005, *ApJ*, in press
- Seager, S. & Sasselov, D. D. 1998, *ApJ*, 502, L157
- Showman, A. P. & Guillot, T. 2002, *A&A*, 385, 166
- Sloan, I. H. & Womersley, R. S. 2001, in *Applied Mathematics Report AMR15-01*, University of New South Wales
- Sozzetti, A., Yong, D., Torres, G., Charbonneau, D., Latham, D. W., Allende Prieto, C., Brown, T. M., Carney, B. W., & Laird, J. B. 2004, *ApJ*, 616, L167
- Steinacker, J., Thamm, E., & Maier, U. 1996, *JQSRT*, 56, 97
- Sudarsky, D., Burrows, A., & Hubeny, I. 2003, *ApJ*, 588, 1121
- Vaz, L. P. R. & Nordlund, A. 1985, *A&A*, 147, 281
- Vidal-Madjar, A., Lecavelier des Etangs, A., Désert, J.-M., Ballester, G. E., Ferlet, R., Hébrard, G., & Mayor, M. 2003, *Nature*, 422, 143